Electronic structures, charge transfer, and charge order in twisted transition metal dichalcogenide bilayers

Yang Zhang ⬤,[*] Tongtong Liu, and Liang Fu

Department of Physics, Massachusetts Institute of Technology, Cambridge, Massachusetts 02139, USA

Moiré superlattices of transition metal dichalcogenide (TMD) bilayers have been shown to host correlated electronic states, which arise from the interplay of long wavelength moiré potential and long-range Coulomb interaction. Here, we theoretically investigate structural relaxation and single-particle electronic structure of twisted TMD homobilayer. From the large-scale density functional theory calculation and continuum model with layer degrees of freedom, we find that the out-of-plane gating field creates a tunable charge transfer gap at the Dirac point between the first and second moiré valence bands. We further study the charge orders at the fractional band fillings. In the flat band limit, we find from Monte Carlo simulations a series of charge-ordered insulating states at various fillings $n = \frac{1}{4}, \frac{1}{3}, \frac{1}{2}, \frac{2}{3}, 1$. We predict that gating field induces a phase transition between different electron crystals at fixed filling $n = \frac{1}{2}$ or $\frac{2}{3}$. At half-filling $n = 1$, the ground state is a Mott insulator with electronically driven ferroelectricity. This work demonstrates that TMD homobilayer provides a powerful platform for the investigation of tunable charge transfer insulator and charge orders.

Moiré superlattices are a fruitful platform for realizing and controlling correlated electron states, as evidenced by the remarkable success in twisted bilayer graphene (TBG) [1–12] and trilayer graphene-hBN heterostructures [13–16]. Recently, a family of moiré materials based on transition metal dichalcogenides (TMDs) [17–29] have attracted great interest. They host an abundance of correlated insulating states at a series of fractional fillings [30–34].

In TMD bilayers, moiré bands are formed from parabolic bands of individual layers. In twisted TMD homobilayers, the moiré bandwidth can be made arbitrarily small by reducing the twist angle, which gives rise to strong correlation without fine tuning. Electrons or holes in these moiré bands are tightly localized in high-symmetry stacking regions, which can be well described by a simple effective tight-binding model. This description offers a convenient starting point for investigating interaction-induced states at finite density. Despite the conceptual simplicity, a quantitative modeling of moiré bands in TMD is highly nontrivial. For example, the moiré bandwidth of TMD heterobilayer WSe_2/WS_2 is only on the order of 10 meV and depends highly on the lattice relaxation [30,31,35,36].

In this paper, using the large-scale density functional theory (DFT), continuum model approach, and Monte Carlo simulation, we study the effect of structural relaxation and electric field on the moiré band structure in twisted TMD homobilayers and predict novel charge order at fractional fillings in the strong-coupling regime. We focus on the moiré valence bands originating from the Γ pocket [37–41]. Due to interlayer tunneling and lattice relaxation, these moiré bands are derived from localized orbitals in MX and XM stacking regions that form a honeycomb lattice. We find a pair of

massless Dirac fermions at K, K' points of the mini-Brillouin zone (BZ), which is protected by the D_3 point group symmetry of the moiré superlattice. Applying an out-of-plane electric field breaks the sublattice symmetry of the honeycomb lattice and opens a tunable gap Δ at the Dirac point. We introduce a continuum model for twisted TMD homobilayers, which captures the layer degrees of freedom and the electrically tunable gap.

We further use an extended Hubbard model on the honeycomb lattice and perform Monte Carlo simulations to study the insulating electron crystals in the flat band limit. We find a distinctive set of charge orders at hole fillings $n = \frac{1}{4}, \frac{1}{3}, \frac{1}{2}, \frac{2}{3}, 1$ on the honeycomb lattice. Interestingly, the charge orders at $n = \frac{1}{2}$ and $\frac{2}{3}$ both break the rotational symmetry and differ from the proposed states in the WSe_2/WS_2 heterobilayer. The $n = 1$ insulating state has a spontaneous out-of-plane ferroelectric polarization, which can be switched by the electric field. These symmetry-breaking charge orders can be directly probed by the optical anisotropy experiments [34,42]. Moreover, we predict that phase transitions between distinct charge-ordered states at the same filling can be induced by the electric field, which tunes the charge-transfer gap Δ. This paper shows that twisted homobilayer MoS_2 provides an ideal platform for investigating electrically tunable charge transfer gap and charge orders.

We study TMD homobilayers with a small twist angle starting from AA stacking, where every metal (M) or chalcogen (X) atom on the top layer is aligned with the same type of atom on the bottom layer [58]. Within a local region of a twisted bilayer, the atom configuration is identical to that of an untwisted bilayer, where one layer is laterally shifted relative to the other layer by a corresponding displacement vector $\mathbf{d}_0$. For this reason, the moiré band structures of twisted TMD bilayers can be constructed from a family of untwisted bilayers at various $\mathbf{d}_0$, all having 1×1
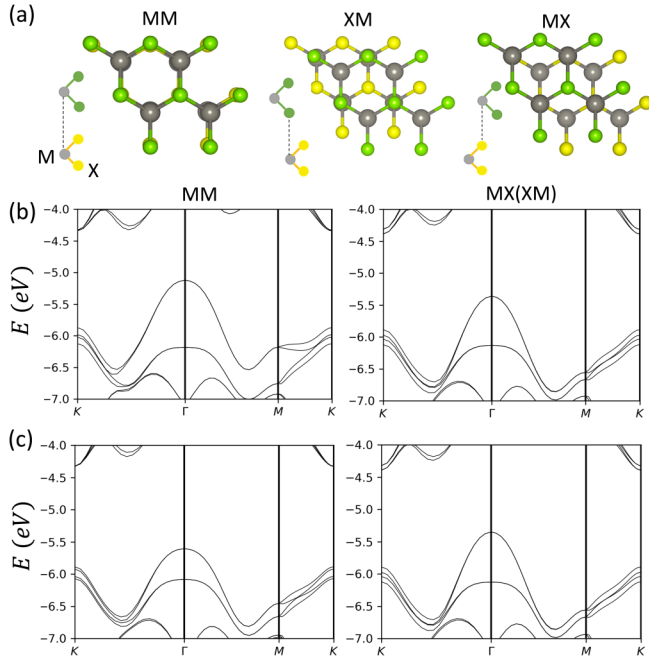
*yzhang11@mit.edu

FIG. 1. (a) Lattice structure of MM, MX, and XM spots for AA stacking heterobilayer; M stands for metal atom, and X stands for chalcogen atom (green for the top layer, yellow for the bottom layer). Density functional theory (DFT) band structures of MM and MX (XM) stacking homobilayer in (b) MoS_2/MoS_2 with identical layer spacing; (c) MoS_2/MoS_2 with relaxed layer spacing.

unit cells. Our analysis thus starts from untwisted bilayers [43].

Specifically, $\mathbf{d}_0 = 0, -(\mathbf{a}_1 + \mathbf{a}_2)/3, (\mathbf{a}_1 + \mathbf{a}_2)/3$, where $\mathbf{a}_{1,2}$ is the primitive lattice vector for untwisted bilayers, corresponding to three high-symmetry stacking configurations of untwisted TMD bilayers, which we refer to as MM, XM, and MX. In MM (MX) stacking, the M atom on the top layer is locally aligned with the M (X) atom on the bottom layer, see Fig. 1(a); likewise for XM. The bilayer structure in these stacking configurations is invariant under threefold rotation around the z axis.

In homobilayer TMD, the spin degenerate Γ pockets in the valence band arise from electron tunneling between the two layers. The kp Hamiltonian takes the form

$$\mathcal{H}(\mathbf{d}_0) = \begin{bmatrix} -\frac{\hbar^2 k^2}{2m^*} + \epsilon_b(\mathbf{d}_0) & \Delta_T(\mathbf{d}_0) \\ \Delta_T^\dagger(\mathbf{d}_0) & -\frac{\hbar^2 k^2}{2m^*} + \epsilon_t(\mathbf{d}_0) \end{bmatrix}. \quad (1)$$

Here, $m^* = 1.07m_e$ is the effective mass for the valence band. Also, $\Delta_T(\mathbf{d}_0)$ is the interlayer tunneling amplitude which depends on the in-plane displacement between the two layers. In contrast to the complex tunneling amplitude for the K pockets [44], here, the time-reversal symmetry at Γ pocket enforces $\Delta_T(\mathbf{d}_0)$ to be real. The potential term $\epsilon_{b,t}(\mathbf{d}_0)$ denotes the energy of the valence band maximum in the absence of tunneling, which arises from the unequal layer weight of the wave function at MX and XM stacking configurations.

We expand $\Delta_T(\mathbf{d}_0)$ in Fourier components up to the second harmonic term:

$$\Delta_T(\mathbf{d}_0) = w_0 + 2w_1 \sum_{j=1}^{3} \cos(\mathbf{G}_j \cdot \mathbf{d}_0)$$
$$+ 2w_2 \sum_{j=1}^{3} \cos(2\mathbf{G}_j \cdot \mathbf{d}_0), \quad (2)$$

where $\mathbf{G}_i (i = 1, 2, 3)$ are the three reciprocal lattice vectors in monolayer TMD. Due to threefold rotational symmetry, Δ_T is a local extremum for MM, MX, and MX stackings, with $\Delta_T = w_0 + 6w_1 + 6w_2$ for $d_0 = 0$ (MM) and $w_0 - 3w_1 - 3w_2$ for $d_0 = \pm(\mathbf{a}_1 + \mathbf{a}_2)/3$ (MX or XM). The zero-momentum-transfer tunneling term w_0 is responsible for the large bonding and antibonding energy splitting for all d_0, while w_1, w_2 capture the variation of the tunneling amplitude at different lateral displacements.

The interlayer tunneling strength depends significantly on the layer spacing d. From the DFT calculation, we find the equilibrium layer spacing of untwisted TMD bilayers in MM, MX, and XM stackings: $d_{MM} = 6.63$ Å and $d_{MX} = d_{XM} = 5.97$ Å. The 10% variation of layer spacing is comparable with that in bilayer graphene [45] and strongly impacts the energy splitting of Γ pockets.

By calculating the work function, we plot in Fig. 1 the band structure of MM- and MX-stacked bilayers, with reference energy $E = 0$ chosen to be the absolute vacuum level. Using the relaxed layer spacings, we find the energy splitting in MX (or XM) stacking to be stronger than in MM, as a result of its smaller layer distance. From the different energy splitting in Fig. 1(c), we obtain the tunneling parameters as $w_0 = 338$ meV, $w1 + w2 = -18$ meV. If the same layer spacing were used for both MX and MM bilayers, the opposite (and incorrect) conclusion about the energy splitting would be found, see Fig. 1(b). Thus, lattice relaxation is crucial for obtaining the correct moiré band structure.

The structure of twisted TMD homobilayers can be described by a lateral shift $\mathbf{d}_0$ that varies slowly in space: $\mathbf{d}_0 = \theta \hat{z} \times \mathbf{r}$. Therefore, we construct the following continuum Hamiltonian for the moiré bands from the Γ pocket two-band kp model:

$$\mathcal{H} = \begin{bmatrix} -\frac{\hbar^2 k^2}{2m^*} + \epsilon_b(r) & \Delta_T(r) \\ \Delta_T^\dagger(r) & -\frac{\hbar^2 k^2}{2m^*} + \epsilon_t(r) \end{bmatrix}. \quad (3)$$

The position-dependent tunneling term is obtained by replacing $\mathbf{d}_0$ with $\theta \hat{z} \times \mathbf{r}$ in Eq. (2):

$$\Delta_T(\mathbf{r}) = w_0 + 2w_1 \sum_{j=1}^{3} \cos\left(\mathbf{G}_j^m \cdot \mathbf{r}\right)$$
$$+ 2w_2 \sum_{j=1}^{3} \cos\left(2\mathbf{G}_j^m \cdot \mathbf{r}\right), \quad (4)$$

where $\mathbf{G}_i^m = \mathbf{G}_i \theta \times \hat{z} (i = 1, 2, 3)$ are the three reciprocal lattice vectors in the moiré superlattice. Likewise, the intralayer potential $\epsilon_{t,b}$ (t, b stand for top and bottom layer, respectively) can be expressed as the first-order Fourier expansion over the
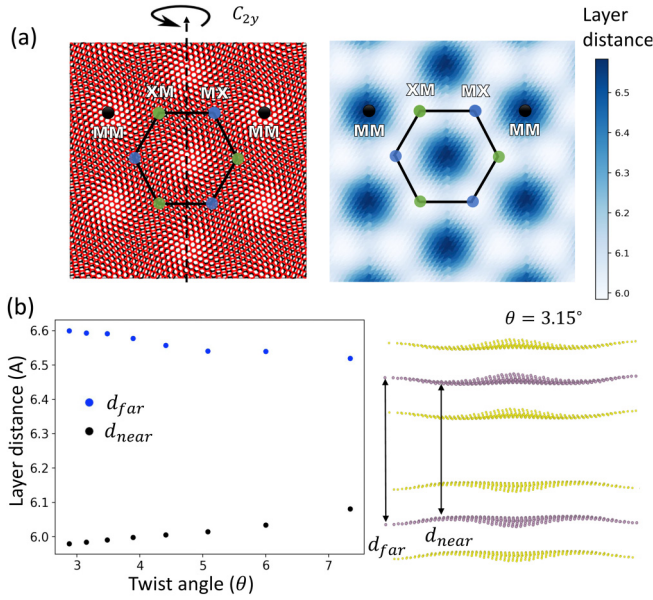
FIG. 2. (a) Real-space moiré pattern of transition metal dichalcogenide (TMD) homobilayer MoS_2, where MM, MX, and XM spots within one supercell are labeled, and the diagram for spatially dependent layer distance (in Å) in the moiré superlattice; (b) twist-angle-dependent layer spacing for d_{far} and d_{near}, and out-of-plane corrugation.

moiré reciprocal lattice vector:

$$\epsilon_{t,b}(\mathbf{r}) = 2V_0 \sum_{j=1,2,3} \cos\left(\mathbf{G}_j^m \cdot \mathbf{r} \pm \phi\right). \quad (5)$$

The sign of phase factor ϕ changes under layer exchange, enforced by C_{2y} symmetry, as shown in Fig. 2(a). The potential term is crucial for the later modeling with out-of-plane gating field.

We now compare the band structure from the continuum model with the large-scale DFT. The moiré superlattice is fully relaxed with van der Waals (vdW) correction incorporated by the vdW-DF (optB86) functionals [46] as implemented in the Vienna *Ab initio* Simulation Package [47]. We plot the twist-angle-dependent layer distance d_{far} in the MM region and d_{near} in the MX (XM) region, in Fig. 2(b). At small twist angle $\theta \sim 0$, the two layers are corrugated, and the layer distance of MM, MX, or XM stacking region approaches that of the untwisted structure. The interlayer tunneling amplitude is maximum at MX and XM regions, which are related by C_{2y} symmetry. As a result, low-energy moiré bands are formed from layer-hybridized orbitals in MX and XM regions, which form a honeycomb lattice with identical onsite potential.

We perform the large-scale DFT simulation to calculate the band structures for various twist angles, shown in Fig. 3. We find that, above a small moiré period $L_m \sim 4.7$ nm with twist angle $\theta = 3.89°$, the two topmost moiré s bands are well separated from the remaining bands. Similar band structures are also found in large-scale DFT calculation with fully relaxed lattice structure for homobilayer MoS_2 [37,38] and WS_2 [39]. Fitting the DFT moiré band structure to the continuum model, we obtain the parameters as $w_0 = 338$ meV, $w_1 = -16$ meV, $w_2 = -2$ meV, $V_0 = 6$ meV, and $\phi = 121°$ at twist angle
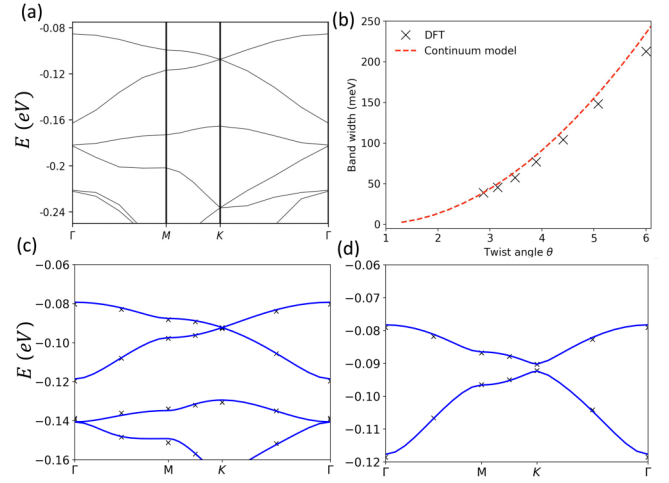

FIG. 3. (a) Density functional theory (DFT) band structure for $\theta = 3.89°$; (b) twist-angle-dependent bandwidth for the first two moiré bands [top two valence bands in (a)] of the honeycomb lattice. DFT (black cross) and continuum model (blue line) band structures for (c) $\theta = 2.876°$; (d) $\theta = 2.876°$ with 0.5 V/nm out-of-plane gating field.

$\theta = 2.876°$. These values are consistent with the estimation from untwisted structures.

As shown in Figs. 3(a) and 3(c), the moiré bands exhibit Dirac points at K and K' points of the moiré BZ. These Dirac points are protected by the D_3 point group of twisted TMD homobilayer: the doublet at K or K' forms a two-dimensional E representation. The bandwidth of Dirac bands changes monotonously from 250 to 10 meV when the twist angle θ ranges from $6°$ to $2°$, as shown in Fig. 3(b). This provides an ideal platform to study the tunable correlation physics of Dirac electrons at the filling of $n = 2$ per moiré unit cell.

In the case of TBG [48], the low energy Dirac fermion is protected by the C_{2z} symmetry, which cannot be broken by the out-of-plane field. However, in MX and XM regions of the twisted homobilayer MoS_2, the wave functions have unequal layer weight, as indicated from the untwisted calculation. Thus, the out-of-plane gating field breaks the C_{2y} symmetry and gaps out the Dirac fermion. A simplified continuum model targeting at antibonding orbitals captures well the topmost moiré bands but cannot describe the band structure and charge distribution involving layer degrees of freedom.

We further calculate the band structure of the fully relaxed moiré superlattice of homobilayer MoS_2 with the applied gating field. As shown in Fig. 3(d), an out-of-plane gating field 0.5 V/nm creates a 2.4 meV gap at the K point, while the bandwidth of the first energy-separable moiré band is 12 meV. At the K point of the band edge, the wave function of the first band is localized at the MX region, while the second band is at the XM region. For small twist angle $\theta = 2°$ with wavelength $L_m = 9.1$ nm, the gating field $E_d = 1$ V/nm induces a charge transfer gap Δ up to 5 meV, even larger than the bandwidth of the topmost moiré band (see Supplementary Material [49]). A larger field-induced Δ can be achieved in twisted TMD homobilayers with reduced interlayer tunneling (which competes with the layer potential asymmetry). This can be realized by inserting an hBN layer in between the top and bottom TMD layers [24].

In the TMD superlattice, the local minimums of the periodic moiré potential can be viewed as the effective moiré atoms to host charge. Under the harmonic approximation, the size of the Wannier orbital for the topmost moiré band is given by $\xi = \sqrt{\frac{\hbar}{m^*\omega}} = 2(\pi)^{-\frac{1}{2}}\sqrt{L_m}(\frac{\hbar^2}{m^*V_m})^{\frac{1}{4}}$ [35] (V_m is the moiré potential integrated to antibonding orbitals). In a homobilayer system without lattice mismatch, the kinetic energy over nearest neighbor interaction (t/V_1) can be tuned arbitrarily small, so that the classical model is well justified at sufficiently small twist angle. The effective extended Hubbard model without kinetic energy is given by

$$H_0 = \sum_{j \in B} \Delta n_j + \sum_i U n_{i\uparrow} n_{i\downarrow} + \frac{1}{2}\sum_{i \neq j} V_{ij} n_i n_j. \quad (6)$$

Here, Δ is the charge transfer gap between two sublattice sites A and B, and V_{ij} is the extended interaction between i and j sites.

In twisted homobilayer MoS_2, the gating field introduces a charge transfer gap Δ. We first discuss the situation with large Δ. At filling $n < 1$, the effective tight-binding model reduces to a triangular lattice model, as in the case of WSe_2/WS_2, and exhibits similar charge order. Various insulating states have been observed at fractional fillings $n = \frac{1}{4}, \frac{1}{3}, \frac{2}{5}, \frac{1}{2}, \frac{3}{5}, \frac{2}{3}$ [30–32]. Due to the strong onsite Coulomb repulsion $U \gg \Delta$, the system at $n = 1$ should be regarded as a charge transfer insulator [35]. When doped to a higher filling $n > 1$, additional charges transfer to the other sublattice and/or layer.

Here, we further study the charge orders of honeycomb lattice with small Δ including $\Delta = 0$ in the flat band limit. We perform classical Monte Carlo simulation up to 120×120 sites with periodic boundary condition for the extended Hubbard model with different gate distances from $d = L_m/2$ to $d = 10L_m$. The distance-dependent interaction strength is plotted in Fig. S2 up to V_{100}, and the interaction cutoff is chosen as $0.1\%V_1$. We identify a series of charge orders at $n = \frac{1}{4}, \frac{1}{3}, \frac{1}{2}, \frac{2}{3}, 1$. For $n < \frac{1}{2}$, moiré electrons are all filled to one sublattice, exhibiting similar charge orders (or generalized Wigner crystals) as observed in WSe_2/WS_2 heterobilayer [30,52,53]).

Interestingly, for small Δ, charge transfer involving two sublattices already takes place for filling $n \geqslant \frac{1}{2}$. At filling factor $n = \frac{1}{2}$, we find an emerging rectangular lattice with $\sqrt{3} \times 2$ periodicity. This state breaks the threefold rotational symmetry and can be viewed as the combination of the stripe states on both sublattices, each at $\frac{1}{4}$ filling. This rectangular electron crystal is energetically favorable compared with the enlarged 2×2 honeycomb crystal at all gate screening distances. In contrast, at large Δ, the ground state becomes a simple stripe state on the triangular sublattice with lower onsite potential, as shown in Fig. 4. We find the critical charge transfer gap is $\Delta_c = 2(V_2 - V_3 - V_4 + 2V_6 - V_9 + V_{12} + ...)$. For $d = L_m = 9.1$ nm, $\Delta_c = 0.12\frac{e^2}{\epsilon L_m} \sim 3.8$ meV can be reached by realistic gating field. We note the critical Δ_c can be further lowered by increasing moiré wavelength.

At filling factor $n = \frac{2}{3}$, the charges form a zigzag stripe order with 6×6 periodicity breaking the C_3 rotational symmetry. This zigzag type charge configuration is energetically favored compared with a linear stripe at screening distances
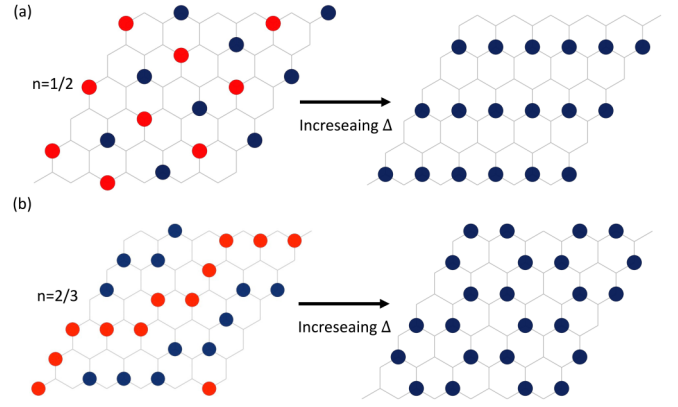

FIG. 4. Ground state charge order at filling (a) $n = \frac{1}{2}$ with increasing charge transfer gap Δ, (b) $n = \frac{2}{3}$ with increasing charge transfer gap Δ.

from $d = \frac{1}{2}L_m$ to $d = 10L_m$. As Δ increases, the zigzag charge stripe transitions to the $\sqrt{3} \times \sqrt{3}$ crystal that occupies one sublattice site only, as shown in Fig. 4. We find the critical charge transfer gap is $\Delta_c = V_2 - V_3 - \frac{10}{3}V_4 + \frac{14}{3}V_5.... = 0.04\frac{e^2}{\epsilon L_m} \sim 1.3$ meV at $d = L_m = 9.1$ nm.

The transition between distinct electron crystals at the same filling is first order. This should lead to a kink in the sublattice and/or layer charge imbalance as a function of the gating field. This prediction, which is a main result of this paper, can be tested in the $MoSe_2/hBN/MoSe_2$ heterostructure [24], where the gating field-induced charge transfer between the top and bottom layers has already been observed at relatively high temperature.

For $n = 1$, we find that, even at $\Delta = 0$, the ground state is a fully sublattice polarized Mott insulating state, which spontaneously breaks the honeycomb lattice symmetry. As the two sublattice sites MX and XM have different layer weight, the Mott insulating state at $n = 1$ develops a finite out-of-plane ferroelectric polarization, which can be switched by the electric field. The ferroelectricity driven by the Mott physics in TMD moiré systems goes beyond the conventional ferroelectricity and enables the fast switching due to electronic origin [50]. For filling $n > 1$, charge-2e trimer can be the lowest energy excitation when tuning the charge transfer gap Δ, providing a platform to design unconventional superconductivity [51].

In homobilayer WSe_2 the valence band maximum is located at K with weak interlayer tunneling amplitude and intralayer potential both on the order of 10 meV. The complex tunneling term between two layers brings further complications for the theoretical and experimental investigation of the insulating states [26,28,44].

In conclusion, we present a combined study of lattice relaxation, single-particle electronic structure, and ground state charge order on the twisted homobilayer MoS_2. Unlike the previous moiré charge transfer insulator in WSe_2/WS_2 heterobilayer, here, out-of-plane gating field breaks C_{2y} symmetry and induces a controllable charge transfer gap. With Monte Carlo simulation, we predict additional stripe-type charge orders at fillings $n = \frac{1}{2}, \frac{2}{3}$ in the emergent honeycomb lattice with $\Delta = 0$. When increasing Δ, these electron crystals transit

to fully sublattice polarized states. We further predict the ferroelectricity at the $n = 1$ Mott insulating state, which enables the ultrafast switching of electronic polarization. This paper demonstrates that the interplay between two moiré regions leads to the charge transfer insulator [35,54] and serves as a platform for creating novel correlated states, such as unconventional density wave [55,56], charge stripes [34], spin superfluid [57], and superconductivity [51].

[1] Y. Cao, V. Fatemi, A. Demir, S. Fang, S. L. Tomarken, J. Y. Luo, J. D. Sanchez-Yamagishi, K. Watanabe, T. Taniguchi, E. Kaxiras, R. C. Ashoori, and P. Jarillo-Herrero, Nature **556**, 80 (2018).

[2] Y. Cao, V. Fatemi, S. Fang, K. Watanabe, T. Taniguchi, E. Kaxiras, and P. Jarillo-Herrero, Nature **556**, 43 (2018).

[3] X. Lu, P. Stepanov, W. Yang, M. Xie, M. A. Aamir, I. Das, C. Urgell, K. Watanabe, T. Taniguchi, G. Zhang, A. Bachtold, A. H. MacDonald, and D. K. Efetov, Nature **574**, 653 (2019).

[4] A. Kerelsky, L. J. McGilly, D. M. Kennes, L. Xian, M. Yankowitz, S. Chen, K. Watanabe, T. Taniguchi, J. Hone, C. Dean, A. Rubio, and A. N. Pasupathy, Nature **572**, 95 (2019).

[5] Y. Jiang, X. Lai, K. Watanabe, T. Taniguchi, K. Haule, J. Mao, and E. Y. Andrei, Nature **573**, 91 (2019).

[6] Y. Xie, B. Lian, B. Jäck, X. Liu, C.-L. Chiu, K. Watanabe, T. Taniguchi, B. A. Bernevig, and A. Yazdani, Nature **572**, 101 (2019).

[7] Y. Choi, J. Kemmer, Y. Peng, A. Thomson, H. Arora, R. Polski, Y. Zhang, H. Ren, J. Alicea, G. Refael, F. von Oppen, K. Watanabe, T. Taniguchi, and S. Nadj-Perge, Nat. Phys. **15**, 1174 (2019).

[8] M. Yankowitz, S. Chen, H. Polshyn, Y. Zhang, K. Watanabe, T. Taniguchi, D. Graf, A. F. Young, and C. R. Dean, Science **363**, 1059 (2019).

[9] E. Codecido, Q. Wang, R. Koester, S. Che, H. Tian, R. Lv, S. Tran, K. Watanabe, T. Taniguchi, F. Zhang, M. Bockrath, and C. N. Lau, Sci. Adv. **5**, eaaw9770 (2019).

[10] A. L. Sharpe, E. J. Fox, A. W. Barnard, J. Finney, K. Watanabe, T. Taniguchi, M. Kastner, and D. Goldhaber-Gordon, Science **365**, 605 (2019).

[11] S. L. Tomarken, Y. Cao, A. Demir, K. Watanabe, T. Taniguchi, P. Jarillo-Herrero, and R. C. Ashoori, Phys. Rev. Lett. **123**, 046601 (2019).

[12] U. Zondiner, A. Rozen, D. Rodan-Legrain, Y. Cao, R. Queiroz, T. Taniguchi, K. Watanabe, Y. Oreg, F. von Oppen, A. Stern, E. Berg, P. Jarillo-Herrero, and S. Ilani, Nature **582**, 203 (2020).

[13] G. Chen, L. Jiang, S. Wu, B. Lyu, H. Li, B. L. Chittari, K. Watanabe, T. Taniguchi, Z. Shi, J. Jung, Y. Zhang, and F. Wang, Nat. Phys. **15**, 237 (2019).

[14] G. Chen, A. L. Sharpe, P. Gallagher, I. T. Rosen, E. J. Fox, L. Jiang, B. Lyu, H. Li, K. Watanabe, T. Taniguchi, J. Jung, Z. Shi, D. Goldhaber-Gordon, Y. Zhang, and F. Wang, Nature **572**, 215 (2019).

[15] M. Serlin, C. Tschirhart, H. Polshyn, Y. Zhang, J. Zhu, K. Watanabe, T. Taniguchi, L. Balents, and A. Young, Science **367**, 900 (2019).

[16] X. Liu, Z. Hao, E. Khalaf, J. Y. Lee, K. Watanabe, T. Taniguchi, A. Vishwanath, and P. Kim, Nature **583**, 221 (2020).

[17] C. Zhang, C.-P. Chuu, X. Ren, M.-Y. Li, L.-J. Li, C. Jin, M.-Y. Chou, and C.-K. Shih, Sci. Adv. **3**, e1601459 (2017).

[18] H. Yu, G.-B. Liu, J. Tang, X. Xu, and W. Yao, Sci. Adv. **3**, e1701696 (2017).

[19] K. L. Seyler, P. Rivera, H. Yu, N. P. Wilson, E. L. Ray, D. G. Mandrus, J. Yan, W. Yao, and X. Xu, Nature **567**, 66 (2019).

[20] K. Tran *et al.*, Nature **567**, 71 (2019).

[21] L. Yuan, B. Zheng, J. Kunstmann, T. Brumme, A. B. Kuc, C. Ma, S. Deng, D. Blach, A. Pan, and L. Huang, Nat. Mater. **19**, 617 (2020).

[22] W. Li, X. Lu, S. Dubey, L. Devenica, and A. Srivastava, Nat. Mater. **19**, 624 (2020).

[23] M. Brotons-Gisbert, H. Baek, A. Molina-Sánchez, A. Campbell, E. Scerri, D. White, K. Watanabe, T. Taniguchi, C. Bonato, and B. D. Gerardot, Nat. Mater. **19**, 630 (2020).

[24] Y. Shimazaki, I. Schwartz, K. Watanabe, T. Taniguchi, M. Kroner, and A. Imamoğlu, Nature **580**, 472 (2020).

[25] Y. Bai, L. Zhou, J. Wang, W. Wu, L. J. McGilly, D. Halbertal, C. F. B. Lo, F. Liu, J. Ardelean, P. Rivera *et al.*, Nat. Mater. **19**, 1068 (2020).

[26] L. Wang, E.-M. Shih, A. Ghiotto, L. Xian, D. A. Rhodes, C. Tan, M. Claassen, D. M. Kennes, Y. Bai, B. Kim *et al.*, Nat. Mater.**19**, 861 (2020).

[27] L. J. McGilly *et al.*, Nat. Nanotechnol. **15**, 580 (2020).

[28] Z. Zhang, Y. Wang, K. Watanabe, T. Taniguchi, K. Ueno, E. Tutuc, and B. J. LeRoy, Nat. Phys. **16**, 1093 (2020).

[29] A. Weston, Y. Zou, V. Enaldiev, A. Summerfield, N. Clark, V. Zólyomi, A. Graham, C. Yelgel, S. Magorrian, M. Zhou *et al.*, Nat. Nanotechnol. **15**, 592 (2020).

[30] E. C. Regan, D. Wang, C. Jin, M. I. B. Utama, B. Gao, X. Wei, S. Zhao, W. Zhao, Z. Zhang, K. Yumigeta, M. Blei, J. D. Carlström, K. Watanabe, T. Taniguchi, S. Tongay, M. Crommie, A. Zettl, and F. Wang, Nature **579**, 359 (2020).

[31] Y. Tang, L. Li, T. Li, Y. Xu, S. Liu, K. Barmak, K. Watanabe, T. Taniguchi, A. H. MacDonald, J. Shan, and K. F. Mak, Nature **579**, 353 (2020).

[32] Y. Xu, S. Liu, D. A. Rhodes, K. Watanabe, T. Taniguchi, J. Hone, V. Elser, K. F. Mak, and J. Shan, Nature **587**, 214 (2020).

[33] X. Huang, T. Wang, S. Miao, C. Wang, Z. Li, Z. Lian, T. Taniguchi, K. Watanabe, S. Okamoto, D. Xiao, S.-F. Shi, and Y.-T. Cui, arXiv:2007.11155.

[34] C. Jin, Z. Tao, T. Li, Y. Xu, Y. Tang, J. Zhu, S. Liu, K. Watanabe, T. Taniguchi, J. C. Hone, L. Fu, J. Shan, and K. F. Mak, arXiv:2007.12068.

[35] Y. Zhang, N. F. Q. Yuan, and L. Fu, Phys. Rev. B **102**, 201115(R) (2020).

[36] H. Li *et al.*, arXiv:2007.06113.

[37] M. H. Naik and M. Jain, Phys. Rev. Lett. **121**, 266401 (2018).

[38] L. Xian, M. Claassen, D. Kiese, M. M. Scherer, S. Trebst, D. M. Kennes, and A. Rubio, arXiv:2004.02964.

[39] M. Angeli and A. MacDonald, arXiv:2008.01735.

[40] Z. Zhan, Y. Zhang, G. Yu, F. G. J. A. Silva-Guillen, and S. Yuan, Phys. Rev. B **102**, 241106 (2020).

[41] S. Venkateswarlu, A. Honecker, and G. T. de Laissardière, Phys. Rev. B **102**, 081103 (2020).

[42] Y. Shimazaki, C. Kuhlenkamp, I. Schwartz, T. Smolenski, K. Watanabe, T. Taniguchi, M. Kroner, R. Schmidt, M. Knap, and A. Imamoglu, arXiv:2008.04156.

[43] S. McDonnell, A. Azcatl, R. Addou, C. Gong, C. Battaglia, S. Chuang, K. Cho, A. Javey, and R. M. Wallace, ACS Nano **8**, 6265 (2014).

[44] F. Wu, T. Lovorn, E. Tutuc, I. Martin, and A. H. MacDonald, Phys. Rev. Lett. **122**, 086402 (2019).

[45] K. Uchida, S. Furuya, J.-I. Iwata, and A. Oshiyama, Phys. Rev. B **90**, 155451 (2014).

[46] J. Klimeš, D. R. Bowler, and A. Michaelides, Phys. Rev. B **83**, 195131 (2011).

[47] G. Kresse and J. Furthmüller, Comput. Mater. Sci. **6**, 15 (1996).

[48] R. Bistritzer and A. H. MacDonald, Proc. Natl. Acad. Sci. **108**, 12233 (2011).

[49] See Supplemental Material at http://link.aps.org/supplemental/10.1103/PhysRevB.103.155142 for the construction of commensurate structures, details of the *ab initio* calculation and continuum model, and additional charge orders.

[50] Z. Zheng, Q. Ma, Z. Bi, S. de la Barrera, M.-H. Liu, N. Mao, Y. Zhang, N. Kiper, K. Watanabe, T. Taniguchi, J. Kong, W. A. Tisdale, R. Ashoori, N. Gedik, L. Fu, S.-Y. Xu, and P. Jarillo-Herrero, Nature **588**, 71 (2020).

[51] K. Slagle and L. Fu, Phys. Rev. B **102**, 235423 (2020).

[52] B. Padhi, C. Setty, and P. W. Phillips, Nano Lett. **18**, 6175 (2018).

[53] B. Padhi, R. Chitra, and P. W. Phillips, Phys. Rev. B **103**, 125146 (2021).

[54] J. Zaanen, G. A. Sawatzky, and J. W. Allen, Phys. Rev. Lett. **55**, 418 (1985).

[55] H. Pan, F. Wu, and S. D. Sarma, Phys. Rev. Research **2**, 033087 (2020).

[56] H. Pan, F. Wu, and S. D. Sarma, Phys. Rev. B **102**, 201104 (2020).

[57] Z. Bi and L. Fu, arXiv:1911.04493.

[58] AB stacking can be viewed as a $180°$ rotation of top layer.

Correction: The caption of Figure 2 contained a minor error and has been fixed.